Three-dimensional shock-sulfur hexafluoride bubble interaction

Cite as: AIP Advances **9**, 115306 (2019); https://doi.org/10.1063/1.5126414
Submitted: 04 September 2019 . Accepted: 25 October 2019 . Published Online: 13 November 2019

Yuejin Zhu, Zhiwei Yang, Longkun Gao, and Kai Hong Luo

Three-dimensional shock-sulfur hexafluoride bubble interaction

Cite as: AIP Advances 9, 115306 (2019); doi: 10.1063/1.5126414
Submitted: 4 September 2019 • Accepted: 25 October 2019 •
Published Online: 13 November 2019

Yuejin Zhu,[1,2,3] Zhiwei Yang,[1] Longkun Gao,[1] and Kai Hong Luo[2,a)]

AFFILIATIONS

[1]School of Energy and Power Engineering, Jiangsu University, Zhenjiang 212013, China
[2]Department of Mechanical Engineering, University College London, Torrington Place, London WC1E 7JE, United Kingdom
[3]State Key Laboratory of Transient Physics, Nanjing University of Science and Technology, Nanjing 210094, China

[a)]**Author to whom correspondence should be addressed:** k.luo@ucl.ac.uk

ABSTRACT

The evolution of shock-sulfur hexafluoride (SF_6) bubble interaction is investigated using a detailed three-dimensional numerical simulation. The influences of the end wall distance on the bubble evolution are analyzed by using the high-resolution simulations. The results show that vorticities mainly emerge at the interfaces of the shock wave and the SF_6 bubble, and a downstream jet is formed, owing to the impingement of the high pressure in the vicinity of the downstream pole of the bubble and the induction of nearby vorticities. Besides, the big vortices of the SF_6 bubble could interact with the walls in the y-direction to increase the bubble volume. When the end wall distance is shortened, a short and wide downstream jet is formed, owing to the untimely interaction of the reflected shock wave with the distorted SF_6 bubble. Also, a new upstream jet emerges behind the impingement of the reflected shock wave, and there is no interaction between the distorted SF_6 bubble and the wall in the y-direction until a very late time. From a quantitative point of view, the discrepancy between the bubble volume and effective bubble volume is larger in the case with a long end wall distance, which has enhanced vorticities and strengthened bubble-wall interaction. Moreover, the reflected shock wave has a dominant compression effect on the distorted SF_6 bubble evolution for the two cases with different end wall distances, but for the case with a longer end wall distance, the bubble-wall interaction has a more significant influence than the influence of vorticities on the bubble volume increase. The computational results demonstrate the three-dimensional effects of shock-SF_6 bubble interactions, which have not been seen in previous two-dimensional simulations.

I. INTRODUCTION

The interaction of a shock wave with a bubble features in a broad range of scientific and engineering applications and has been used widely as a canonical reference system to test new numerical methods for compressible interfacial flows.[1] Even so, the many complicated physics and chemical processes involved have not been fully understood at present.

During the shock-bubble interaction, the ambient unshocked gas has density ρ_1 and the unshocked bubble gas has density ρ_2; thus, an Atwood number $At = (\rho_2 - \rho_1)/(\rho_2 + \rho_1)$ can be defined. For the $At < 0$ case (the bubble gas is lighter than the ambient gas), the transmitted shock wave inside the bubble propagates faster than the outside incident shock (IS) wave. While the $At > 0$ case shows the converse effect, that is, the transmitted shock wave propagates slower than the incident shock wave, the transmitted shock wave may focus at the downstream pole of the bubble and collapse into a single shock-focusing point with high pressure. In the last few decades, lots of relevant experimental and numerical studies have been conducted. Haas and Sturtevant[2] performed detailed experimental investigations into the shock-bubble interaction, and helium (He) and chlorodifluoromethane (R22) were adopted as the bubble gas. Although the bubble evolution under the shock acceleration was obtained in their work, only one photograph was taken during each run; hence, the experimental repeatability was not good enough. Then, Layes *et al.*[3–5] experimentally studied bubble deformations of different gases [He, nitrogen (N2), and krypton (Kr)] via flow visualization techniques. The changes in the characteristic bubble sizes were measured, and the influence of the initial shock Mach number (Ma) on the evolution of different gas bubbles was also analyzed.

During the same period, with the aid of the planar laser diagnostics, the unstable evolution of a He bubble subjected to a planar shock wave in ambient nitrogen was studied by Ranjan *et al.*,[6,7] and the different vortex rings of the distorted He bubble were investigated. In recent years, Si *et al.*[8] conducted a number of experimental sets of He and sulfur hexafluoride (SF_6) bubbles surrounded by air using the high-speed Schlieren photography with high time-resolutions, and the differences between the two gas bubbles were studied. Also, distinct flow structures were observed due to the additional vorticity and wave configuration caused by the reshock.[8]

In addition to the aforementioned experimental works, a wealth of numerical studies have been performed on shock-bubble interaction. In 2008, Niederhaus *et al.*[9] conducted the three-dimensional Eulerian simulations to study the morphology and time-dependent integral properties of shock-bubble interaction. The influences of different Atwood numbers ($-0.8 < At < 0.7$) and incident shock intensity ($1.1 < Ma \leq 5.0$) were investigated, and the time-dependent volumetric compression, circulation, and extent of mixing in the shocked-bubble flow were analyzed. However, they also found that the three-dimensional effects were relatively insignificant with the increasing incident shock intensity.[7] In the same year, Fu *et al.*[10] numerically studied the flow characteristics after the interaction of a planar shock with a light bubble ($At < 0$) by solving the three-dimensional compressible Navier-Stokes (N-S) equations, and the distortion of the incident shock wave and the bubble was discussed. Subsequently, Zhu *et al.*[11] numerically investigated the interaction between a shock wave and a He bubble using the large eddy simulation (LES) method. The evolution of vortex rings and the influence of the incident shock wave intensity were analyzed in detail. Moreover, Hejazialhosseini *et al.*,[12] Rybakin and Goryachev,[13] and Yang *et al.*[14] also conducted numerical research on the interaction between a shock wave and a spherical He bubble, and the bubble deformation and the evolution of vortex rings were discussed.

It is worth noting that previous three-dimensional numerical studies were mainly concentrated on cases with $At < 0$. Actually, due to the different densities inside and outside the gas bubble, the evolution of the shock wave and the gas bubble shows a completely different trend for $At > 0$ cases. Take the particular SF_6 gas bubble as an example; a distinct SF_6 jet can occur at the bubble interface after the impingement of the incident shock wave under a proper initial condition. In recent years, Zhai *et al.*[15,16] and the present authors[17–19] have made several efforts to reveal the detailed evolution of the distorted SF_6 gas bubble and the jet formation mechanism, but these studies were all using two-dimensional simulations. In view of the bubble interface instability being intrinsically nonlinear and three-dimensional, a three-dimensional numerical simulation is needed for the study of the shock-SF_6 bubble interaction. Moreover, the reflected shock (RS) wave can interact with the distorted bubble again. The interactions of the bubble with the incident shock wave and its reflected shock wave would further promote the instability of the bubble interface and therefore make the shock-bubble interaction process more complicated. Hence, it is expected that a three-dimensional numerical simulation of the multiple interactions among the SF_6 bubble, the incident shock wave, and its reflected shock wave can gain more fundamental insights into the instability and evolution of the SF_6 bubble interface. Thus, in this study, SF_6 is adopted as the heavy bubble gas, and a highly accurate numerical scheme is employed. The evolution of the three-dimensional distorted SF_6 gas bubble and shock wave is presented and analyzed in detail, and the influence of the reflected shock wave on the bubble deformation process is also scrutinized.

II. NUMERICAL METHOD AND SETUP

A. Numerical method

The three-dimensional Navier-Stokes (N-S) equations are adopted in this study, which can be expressed as

$$\frac{\partial \rho}{\partial t} + \frac{\partial}{\partial x_j}(\rho u_j) = 0, \tag{1}$$

$$\frac{\partial \rho u_i}{\partial t} + \frac{\partial}{\partial x_j}(\rho u_i u_j) = -\frac{\partial p}{\partial x_i} + \frac{\partial \tau_{ij}}{\partial x_j}, \tag{2}$$

$$\frac{\partial E}{\partial t} + \frac{\partial}{\partial x_j}(u_j E + p u_j) = -\frac{\partial q_j}{\partial x_j} + \frac{\partial}{\partial x_j}(u_i \tau_{ij}), \tag{3}$$

$$\frac{\partial \rho Y}{\partial t} + \frac{\partial}{\partial x_j}(\rho Y u_j) = \frac{\partial}{\partial x_j}\left(D\rho \frac{\partial Y}{\partial x_j}\right), \tag{4}$$

where ρ is the density; u_j is the jth velocity component (j = 1, 2, and 3); p is the pressure; τ_{ij} is the viscous stress tensor, $\tau_{ij} = \rho\upsilon(\frac{\partial u_i}{\partial x_j} + \frac{\partial u_j}{\partial x_i} - \frac{2}{3}\delta_{ij}\frac{\partial u_k}{\partial x_k})$, where υ is the kinematic viscosity and δ_{ij} is the Kronecker function; E is the total energy per unit volume, $E = p/(\gamma - 1) + 0.5\rho \sum_{i=1}^{3} u_i^2$, where γ is the adiabatic index; q_j is the heat flux, which can be expressed as $q_j = -k\partial T/\partial x_j$, where k and T are the thermal conductivity and temperature, respectively; Y is the mass fraction of the ambient gas; and D is the diffusion coefficient. Furthermore, the values of υ, k, and D are given according to the ambient gas properties.[18]

To solve the three-dimensional N-S equations, a ninth-order weighted essentially nonoscillatory (WENO) scheme[20] is utilized to discretize the inviscid parts of the flux terms, and a tenth-order central difference scheme is used to solve the viscous parts. Also, the third-order Runge-Kutta method is employed in time advancing.

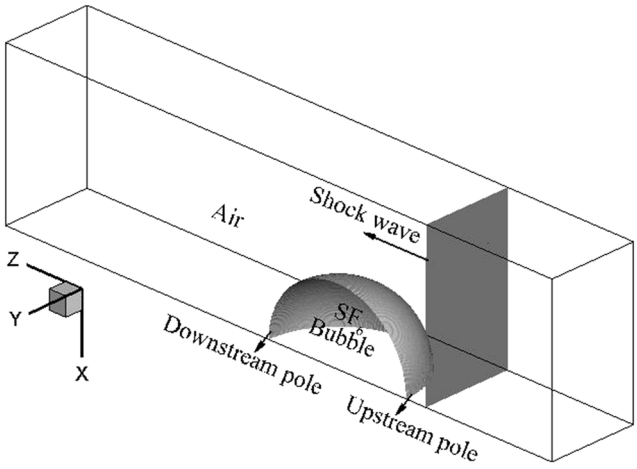

FIG. 1. Computational domain and initial conditions.

TABLE I. Physical properties of the used gas.

Gas	Density (kg m^{-3})	Specific heat ratio	Sound speed (m s^{-1})	Acoustic impedance (kg m^{-2} s^{-1})	Molecular weight
Air	1.19	1.4	346	411.7	29
SF_6	6.03	1.1	135	814	146

B. Computational setup

To reduce the computation cost, a quarter-spherical bubble is simulated on a uniform Cartesian grid (grid size $\Delta x = \Delta y = \Delta z = 0.2$ mm) in a three-dimensional domain (35 mm × 20 mm × 130 mm, corresponding to x-y-z directions), as shown in Fig. 1. The initial x-y planar shock wave (Ma = 1.21) propagates along the z-direction, and it impinges on the initial spherical SF_6 gas bubble with a diameter of $D_0 = 32.5$ mm and initial pressure of $P_0 = 101\,325$ Pa. Then, the incident shock wave reflects from the end of the computational domain in the z-direction, which impinges on the distorted SF_6 bubble again. In this study, two cases with different values of the end wall distance L are investigated, and L is measured from the SF_6 bubble center to the end wall in the z-direction. Specifically speaking, $L = 79$ mm is adopted in case 1, $L = 27$ mm in case 2, and the other initial conditions are the same in the two cases. Moreover, the physical properties of the chosen gases are given in Table I.

For the boundary conditions, the inflow boundary condition at the right $z = 0$ mm plane is imposed, and the left, rear, and upper planes employ the no-slip wall conditions. Besides, symmetry boundary conditions are applied at the two cut surfaces of the bubble (the front and bottom planes).

III. RESULTS AND DISCUSSION

A. Numerical validation

To demonstrate the reliability of the adopted numerical method and grid size, the numerical results of the interaction between the planar shock wave and the spherical SF_6 gas bubble are compared with the experimental results of Si *et al.*[8] The computational Schlieren results of the x-z plane are obtained by Eq. (5), which is written as[21]

$$I_{x\text{-}z} = \left[\left(\int \frac{\partial \rho}{\partial x} \mathrm{d}y\right)^2 + \left(\int \frac{\partial \rho}{\partial z} \mathrm{d}y\right)^2\right]^{\frac{1}{2}}, \tag{5}$$

where $I_{x\text{-}z}$ is the light intensity decrease of the computational x-z plane. Figure 2 presents the comparisons between the experimental Schlieren images and the present computational Schlieren results at the selected time instants, where Figs. 2(a) and 2(b) correspond to the time period behind the incident shock wave impingement and Figs. 2(c) and 2(d) correspond to the interaction between the distorted SF_6 bubble and the reflected shock wave. The result shows that the initial spherical SF_6 bubble is compressed by the incident shock wave in Fig. 2(a). Simultaneously, the refracted shock within the SF_6 bubble propagates more slowly than the outside incident shock, which forms an undisturbed zone (UZ) near the downstream interface of the SF_6 bubble. Then, owing to the complicated pressure distribution in the SF_6 bubble, a downstream SF_6 jet forms behind the incident shock wave, and the curvature of the curved incident shock wave affected by the different acoustic impedance of SF_6 and air decreases in Fig. 2(b). During the interaction between the reflected shock wave and the distorted bubble, a slender downstream jet is found in Fig. 2(c), and the reflected shock wave interacts with the jet at this time instant. Eventually, the reflected shock wave has passed through the distorted bubble completely in Fig. 2(d), and the SF_6 bubble is further compressed and more vorticities emerge throughout the distorted bubble interface. From Fig. 2, it is easy to find that good qualitative agreement between the experimental and the computational results is obtained, and the resolution can correctly capture the evolution of the SF_6 bubble and the shock wave, which implies that the numerical method and grid size are reliable and acceptable in this three-dimensional study.

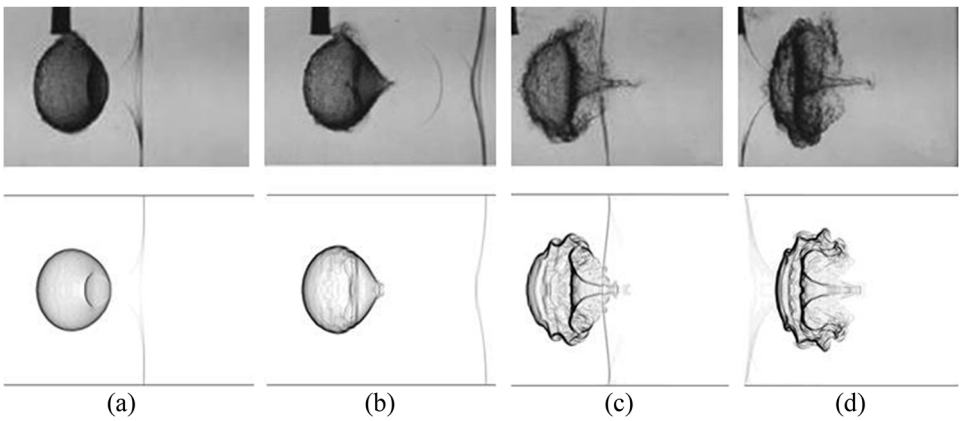

FIG. 2. Comparisons between the experimental[8] and the present computational results: (a) $t = 118.5$ μs, (b) $t = 195.3$ μs, (c) $t = 393.2$ μs, and (d) $t = 500.7$ μs.

B. Incident shock wave-SF_6 bubble interaction (case 1)

Figure 3 shows the interaction between the incident shock wave and the SF_6 gas bubble at the y = 20 mm plane of different time instants in case 1 (L = 79 mm), where the top half contour of each inset presents the vorticity magnitude ($|\omega| = \sqrt{\omega_x^2 + \omega_y^2 + \omega_z^2}$, where ω_x, ω_y, and ω_z are the vorticities in each direction, respectively), the bottom half contours represent the density, and the black lines represent the pressure isolines. Due to the large acoustic impedance in the SF_6 bubble, the refracted shock wave inside the bubble propagates slower than the outside incident shock wave, and an undisturbed zone (UZ) is formed by the curved refracted shock wave and the downstream bubble interface in Fig. 3(a). At this time, the vorticities mainly emerge at the interfaces of the shock and the compressed SF_6 bubble. Especially for the top and bottom interface of the bubble, the baroclinic effect owing to the misalignment between the pressure and density gradients is the strongest, which is beneficial for the production of vorticities. Subsequently, the inner refracted shock wave converges in the vicinity of the downstream SF_6 bubble interface, so UZ shrinks with a pronounced pressure increase in Fig. 3(b), and this phenomenon can be called the shock focusing. The final shock focusing state is during the time between 147.9 μs and 195.3 μs, which is not shown here. In Fig. 3(c), the high pressure zone owing to the shock focusing begins to expand to impinge on the downstream bubble interface, and small vorticities can be found near the downstream interface of the bubble. Finally, the high pressure impingement and the induction of the downstream vorticities can both promote the formation of the downstream jet in Fig. 3(d), which is in accordance with our previous study.[17]

As time goes by, the SF_6 bubble deforms continuously behind the incident shock wave in the flow field. To investigate the three-dimensional deformation of the distorted SF_6 bubble, Fig. 4 presents the complicated three-dimensional SF_6 bubble structure at t = 356.6 μs, where Fig. 4(a) corresponds to the half-cutaway view and Fig. 4(b) corresponds to the global view. The complicated SF_6 bubble structure is represented by the isosurface of the mass fraction of the ambient gas, where the blue color means Y = 0.01, the green color means Y = 0.5, and the red color means Y = 0.99. The different values of Y imply the different mixing degrees between the ambient air and the SF_6 gas. The larger the value of Y, the stronger the mixing degree. It should be noted that the reflected shock wave does not impinge on the distorted SF_6 bubble again at this time instant. From Fig. 4, it is clear to observe the corrugation and vortices of the SF_6 bubble interface owing to the incident shock impingement, and a distinct downstream jet evolves in the flow field. Furthermore, at the headmost of the jet, there also exist small vortices which can promote the stretch of the jet, especially for the $Y \geq 0.5$ condition. On the other hand, the big vortices on the top and bottom of the SF_6 bubble interact with the walls, owing to the small size in the y-direction, and this interaction could induce an obvious increase in the bubble volume, which reflects the influence of the three-dimensional computation in this study to an extent.

C. Reflected shock wave-SF_6 bubble interaction (case 1)

When the reflected shock (RS) wave interacts with the distorted SF_6 bubble again, a more complicated deformation occurs. To depict this, Fig. 5 gives the interaction between the reflected shock wave and the distorted SF_6 gas bubble at the y = 20 mm plane of different time

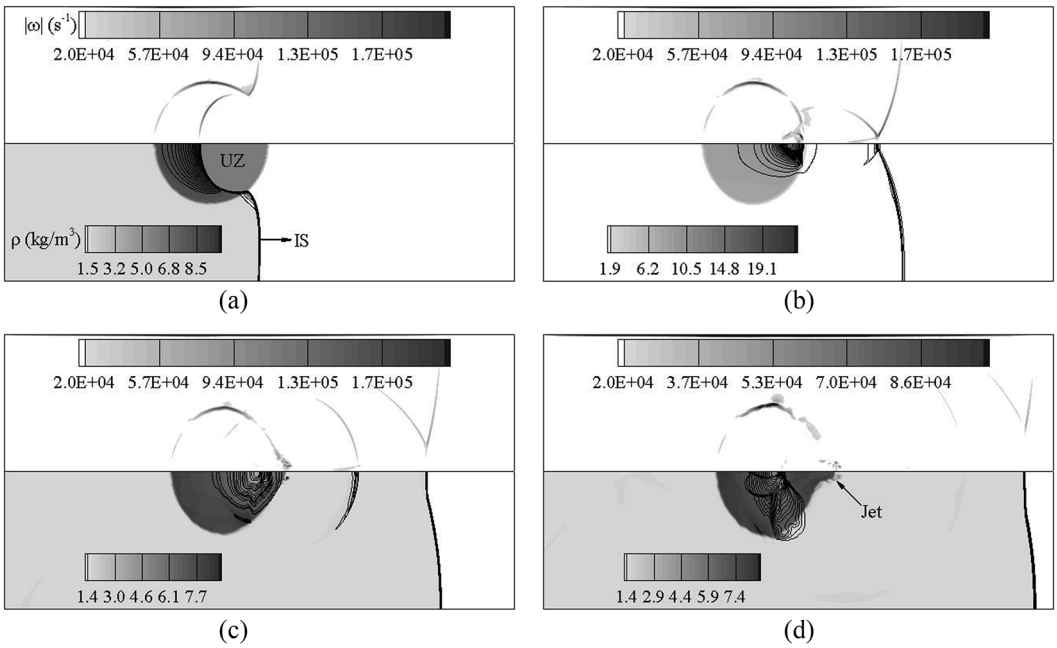

FIG. 3. Evolution of the incident shock wave and the SF_6 gas bubble (y = 20 mm plane): (a) t = 83.7 μs, (b) t = 147.9 μs, (c) t = 195.3 μs, and (d) t = 229.8 μs.

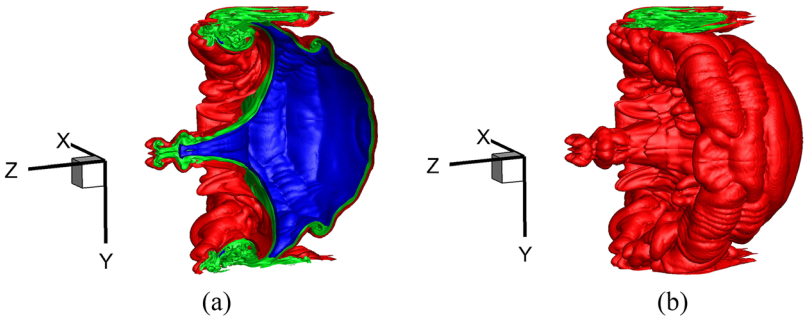

FIG. 4. Three-dimensional SF_6 bubble structure at t = 356.6 μs: (a) half-cutaway view and (b) global view.

instants, and the representation method is the same as that in Fig. 3. In Fig. 5(a), the RS begins to impinge on the jet, and the vorticities mainly deposit on the top and bottom interfaces of the distorted SF_6 bubble, where vortices with different sizes are found. With the propagation of RS, the vorticities on the jet are strengthened in Fig. 5(b). Actually, in accordance with the baroclinic effect, vortices produced by the RS impingement are of the opposite rotational direction compared with the original vortices. When the RS impinges on the compressed and distorted SF_6 bubble, due to the bubble shape and the difference in the acoustic impedance, a curved reflected refracted shock (RTS) and a reflected diffracted shock (RDTS) emerge inside the bubble at t = 459.1 μs. As time goes by, the RS further compresses the distorted SF_6 bubble, and the bubble volume decreases obviously in Fig. 5(d). In short, more vorticities emerge on the bubble interface during the interaction between the RS and the distorted SF_6 bubble.

To better depict the three-dimensional deformation of the distorted SF_6 bubble during the interaction between the reflected shock wave and the SF_6 gas bubble, Fig. 6 shows the complicated three-dimensional SF_6 bubble structure corresponding to the time instants in Fig. 5, where the structure representation method is the same as that in Fig. 4. In Fig. 6(a), the reflected shock wave begins to impinge on the jet [as shown in Fig. 5(a)], and the bubble interface exhibits corrugation and vortices, owing to the incident shock wave impingement. Meanwhile, the distorted SF_6 bubble also interacts with the y = 0 mm wall. With the impingement of the reflected shock wave in Figs. 6(b)–6(d), the distorted bubble is compressed obviously, and more vortices and corrugation can be found at the SF_6 bubble interface. Also, due to the interaction between the distorted bubble and the wall, the bubble area on the y = 0 mm wall increases greatly.

When the reflected shock wave has passed through the SF_6 bubble completely, the distorted bubble continues to deform in the flow field. Figure 7 further presents the complicated three-dimensional SF_6 bubble structure at t = 612 μs by using the same structure representation method as above, where Fig. 7(a) corresponds to the half-cutaway view and Fig. 7(b) corresponds to the right side view. It is found that the red isosurface of Y = 0.99 is much larger than the green and blue isosurfaces, which indicates that the mass is stripped away from the original SF_6 bubble, and the mixing between the

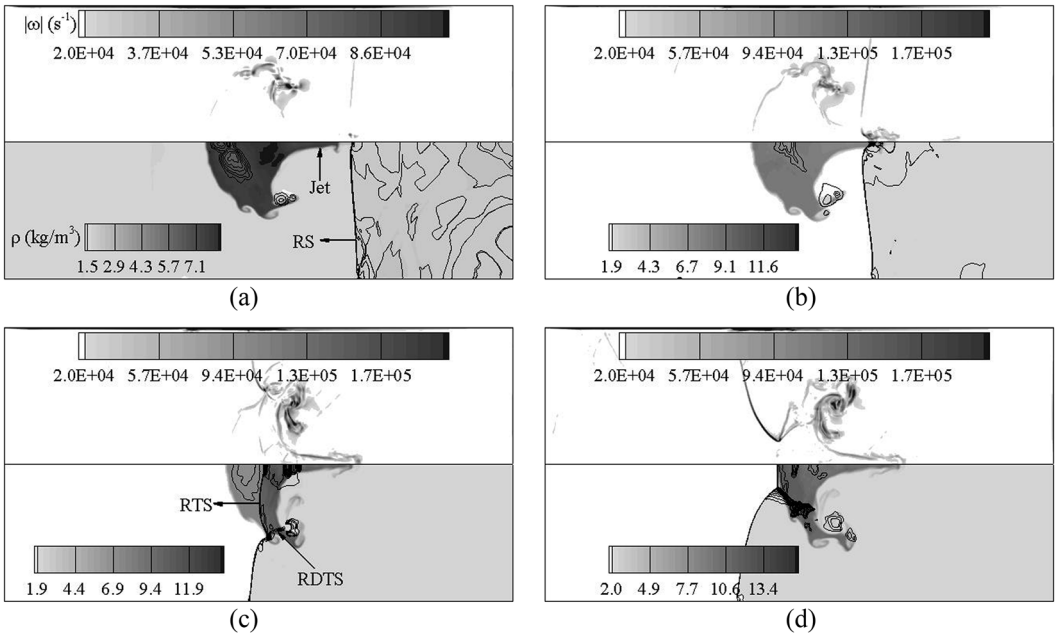

FIG. 5. Evolution of the reflected shock wave and the SF_6 gas bubble (y = 20 mm plane): (a) t = 372.1 μs, (b) t = 393.2 μs, (c) t = 459.1 μs, and (d) t = 500.7 μs.

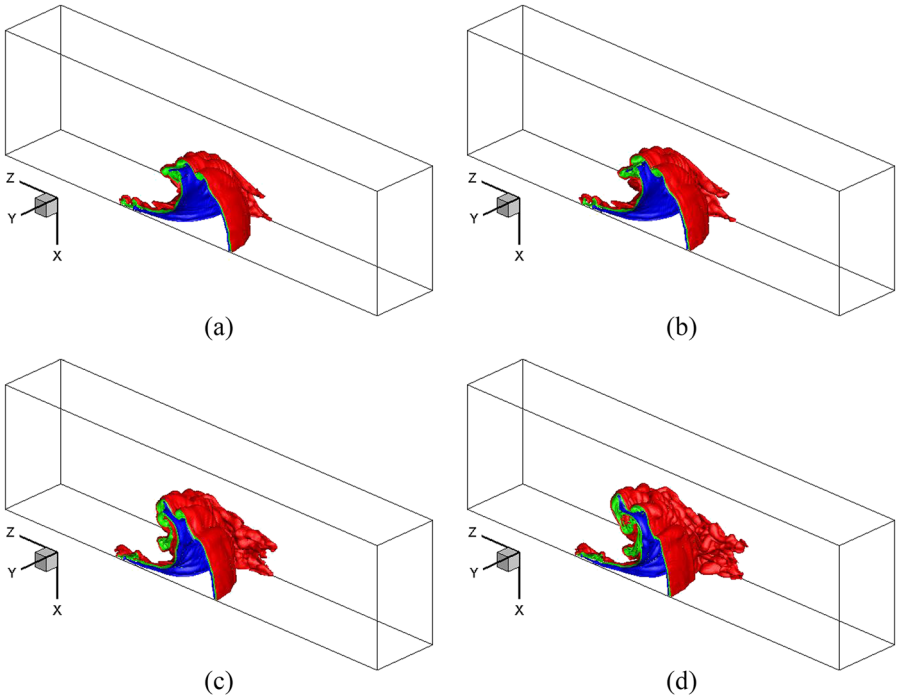

FIG. 6. Three-dimensional SF_6 bubble structure during the interaction between the reflected shock wave and the SF_6 gas bubble: (a) t = 372.1 μs, (b) t = 393.2 μs, (c) t = 459.1 μs, and (d) t = 500.7 μs.

ambient air and the SF_6 gas is relatively strong at this time instant. From the view of green and blue isosurfaces, the distorted SF_6 bubble is further compressed, and two distinct pairs of vortices emerge on the headmost and adjacent locations of the jet (from the isosurface of Y = 0.5). Also, the big vortices on the top and the bottom of the distorted SF_6 bubble continue to interact with the walls in the y-direction, and an obvious increase in the bubble volume is observed, which reflects the influence of the three-dimensional computation in this study. It is worth noting that no jet forms in the upstream interface of the distorted SF_6 bubble after the impingement of reflected shock in this case.

D. Influence of end wall distance (case 2)

If the end wall distance L reduces, the reflected shock wave will impinge on the distorted SF_6 bubble earlier, so the deformation degree of the bubble is smaller than that in case 1 and therefore induces a different evolution process of the bubble and the shock wave. To compare the numerical results with different end wall distances, case 2 is constructed in this study, where all the initial conditions remain unchanged compared with those in case 1 expect the L reduces from 79 mm to 27 mm.

Figure 8 presents the interaction between the incident and reflected shock waves and the SF_6 gas bubble at the y = 20 mm plane of different time instants in case 2, and the representation method is the same as that in Figs. 3 and 5. In Fig. 8(a), a same undisturbed zone (UZ) is formed by the curved refracted shock wave and the downstream bubble interface, and the vorticities mainly emerge at the interface of the shock and the compressed SF_6 bubble. However, the incident shock (IS) wave has interacted with the right solid wall at this time instant. Consequently, the UZ shrinks with a pronounced pressure increase in Fig. 8(b), and the reflected shock (RS) wave has formed. In Fig. 8(c), the RS moves from right to left to impinge on the distorted SF_6 bubble again, and a new expanding shock wave named TES is generated, which is mainly because of the expansion of the high pressure zone during the shock

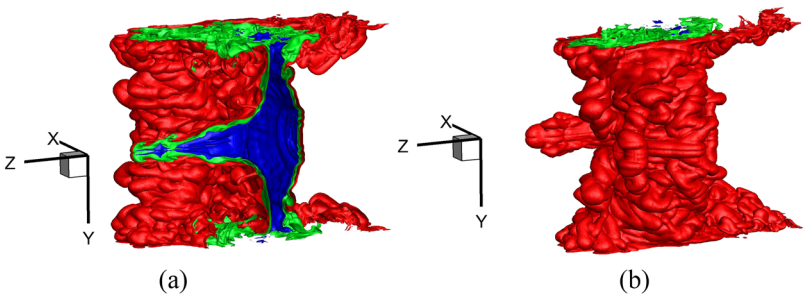

FIG. 7. Three-dimensional SF_6 bubble structure at t = 612 μs: (a) half-cutaway view and (b) right side view.

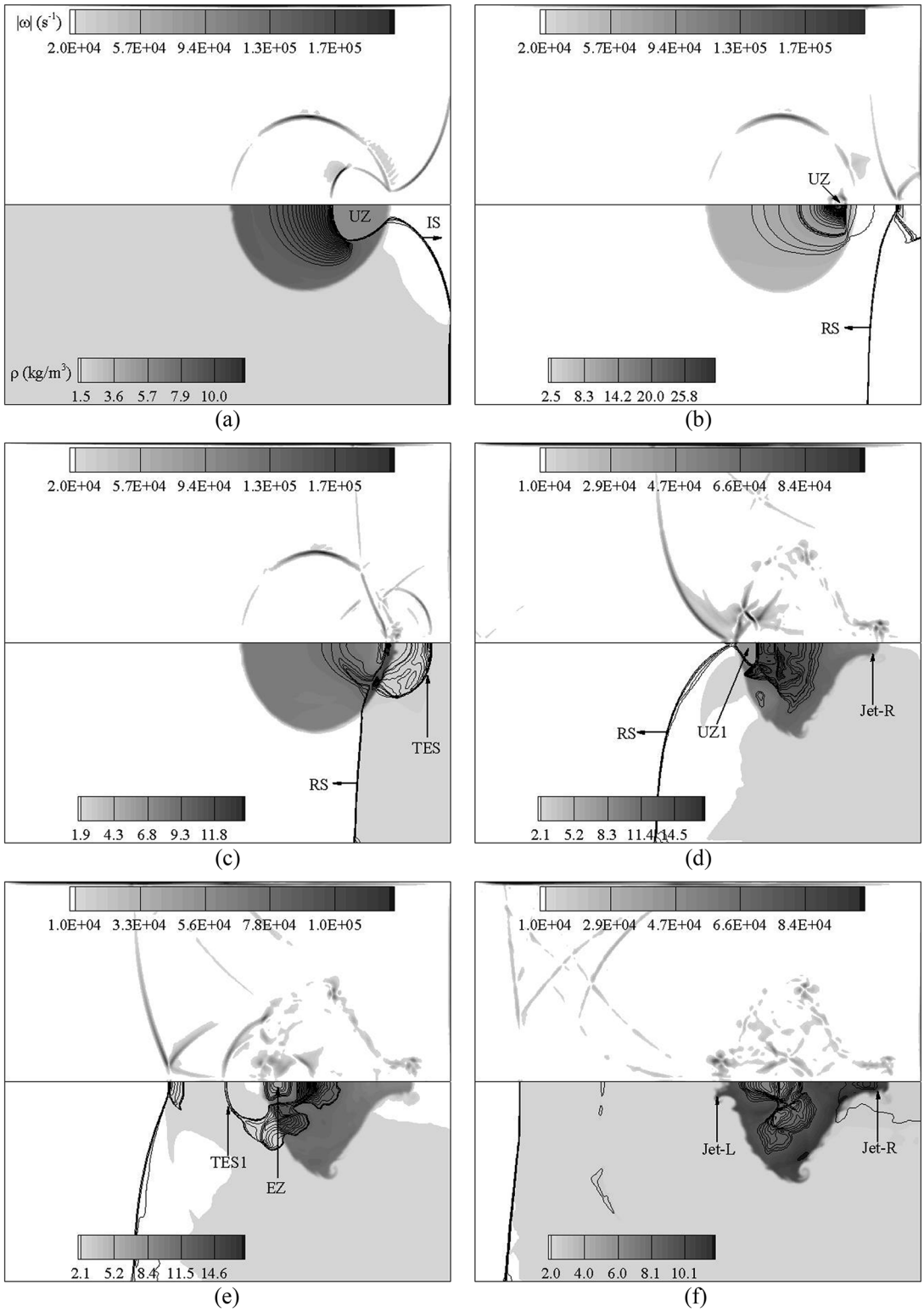

FIG. 8. Evolution of the incident and reflected shock waves and the SF_6 gas bubble (y = 20 mm plane): (a) t = 116 μs, (b) t = 143.2 μs, (c) t = 167.1 μs, (d) t = 265.1 μs, (e) t = 294.3 μs, and (f) t = 349.4 μs.

focusing process in the vicinity of the downstream of the SF_6 bubble. Meanwhile, small vorticities can be found near the downstream interface of the bubble under the integrated effects of the reflected shock wave and the high pressure zone during the incident shock focusing process. The high pressure impingement and the vorticity induction promote the formation of the rightward jet (Jet-R) in Fig. 8(d). Moreover, at this time instant, the RS has passed through the distorted SF_6 bubble, and a similar undisturbed zone (UZ1) of the RS forms. Later, the UZ1 shrinks to complete a new shock focusing process to form a new high pressure zone, which will continue to expand to form the expanding zone (EZ), and a new expanding shock wave named TES1 is generated following the RS in Fig. 8(e). Finally, a new leftward jet (Jet-L) can be found in Fig. 8(f), owing to the complicated shock impingement and vorticity induction. Compared with the results in case 1, two distinct SF_6 jets (Jet-L and Jet-R) emerge simultaneously behind the reflected shock wave. This is mainly attributed to the fact that the distorted SF_6 bubble in case 1 becomes more flat, which weakens the reflected shock focusing effect in the distorted bubble. Furthermore, owing to the short end wall distance in case 2, the reflected shock wave impinges on the distorted SF_6 bubble during the budding stage of the Jet-R formation, which induces a short and wide jet compared with that in case 1.

To clearly show the three-dimensional deformation of the distorted SF_6 bubble in case 2, Fig. 9 shows the complicated three-dimensional SF_6 bubble structure corresponding to the selected time instants in Fig. 8, where the structure representation method is the same as that in Figs. 4, 6, and 7. In Fig. 9(a), the SF_6 bubble interface remains basically spherical, which means the compression of the incident shock is not obvious, but at this time instant, it is found that some distortion emerges downstream of the bubble interface. This is because the SF_6 bubble interface is affected by the impingement of the high pressure zone during the shock focusing process inside the bubble and the reflected shock wave simultaneously, which can be shown in Fig. 8(c). Furthermore, under the influence of the earlier impingement of the reflected shock wave, a short and wide jet emerges in Fig. 9(b), while the bubble interface also exhibits corrugation due to the reflected shock wave impingement. As shown in Fig. 8, there is also a high pressure zone emerging in the vicinity of the upstream of the bubble; thus, a jet following the reflected shock wave is formed, as shown in Figs. 9(c) and 9(d). It should be noted that in case 2, due to a shorter end wall distance, not only a distinct variation in the jet formation is observed, but also no interaction occurs between the distorted SF_6 bubble and the wall in the y-direction until this time instant. Hence, it is expected that the bubble volume is smaller than that in case 1.

The distorted SF_6 bubble continues to deform in the flow field behind the reflected shock wave. Figure 10 further presents the complicated three-dimensional SF_6 bubble structure at t = 362.3 μs by using the same structure representation method as above, where Fig. 10(a) corresponds to the half-cutaway view and Fig. 10(b) corresponds to the global view. It is found that the SF_6 bubble shows distinct corrugation for every isosurface of the different mass fraction of the ambient gas, and there are two short and wide jets emerging on the distorted SF_6 bubble interface. Besides, small vortices are shown on the surface of the jets. A big vortex pair also forms on the top and the bottom of the bubble, which begins to interact with the wall to enhance the bubble volume to an extent.

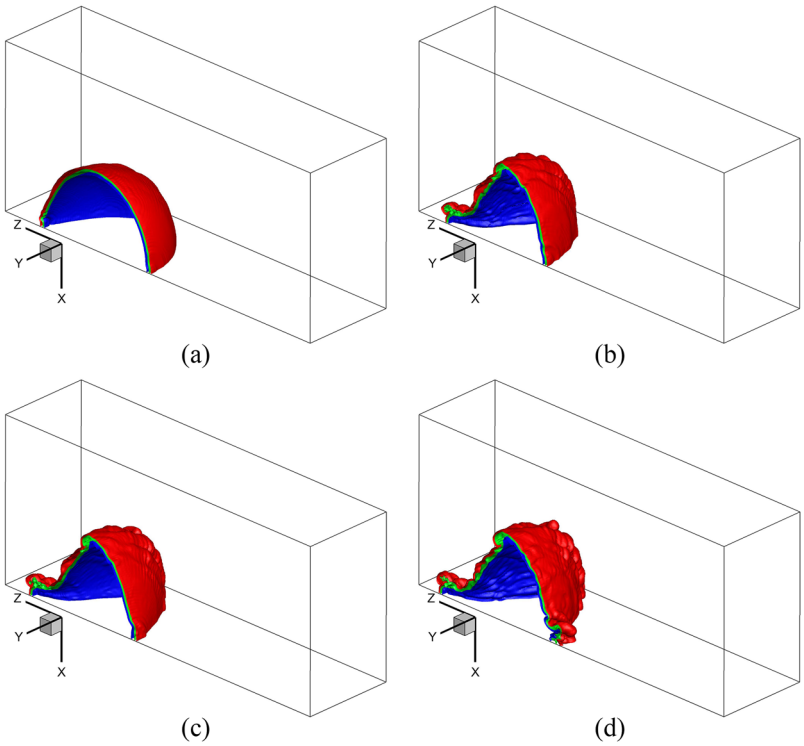

FIG. 9. Three-dimensional SF_6 bubble structure during the interaction between the incident and reflected shock waves and the SF_6 gas bubble: (a) t = 167.1 μs, (b) t = 265.1 μs, (c) t = 294.3 μs, and (d) t = 349.4 μs.

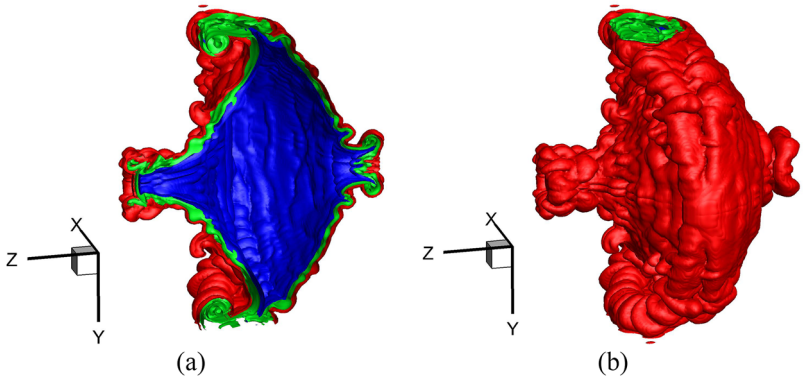

FIG. 10. Three-dimensional SF_6 bubble structure at t = 362.3 μs: (a) half-cutaway view and (b) global view.

E. Evolution of SF_6 bubble volume in the two cases

As shown above, the SF_6 bubble undergoes complicated deformation during the impingement of the incident and reflected shock waves. In order to further investigate the evolution of SF_6 bubble volume in the two different cases, the bubble volume V and effective bubble volume V_{eff} (the influence of air is eliminated) are defined as follows:

$$V = \int_B dV, \tag{6}$$

$$V_{eff} = \int_D (1 - X) dV, \tag{7}$$

where the subscript B represents the bubble zone, D represents the entire computational domain, and X is the air volume fraction.

Figure 11 shows the evolution of the dimensionless V/V_0 and V_{eff}/V_0 with time (V_0 is the initial bubble volume). In this figure, I_{in} indicates the incident shock compression stage for the two cases, $I_{re,1}$ indicates the reflected shock compression stage for case 1, and $I_{re,2}$ indicates the reflected shock compression stage for case 2. Besides, the short solid lines with different colors represent the variation rate of V/V_0 and V_{eff}/V_0 during different time periods, and the same color means the same value. For case 1, owing to the complicated pressure disturbance inside the SF_6 bubble, the value of the effective bubble volume shows a small oscillation around an average value between I_{in} and $I_{re,1}$, while the value of the bubble volume increases gradually, which means the vorticities emerging on the SF_6 bubble interface and the distorted bubble interacting with the wall both have influences on the increase in the bubble volume. Furthermore, for the time period behind the $I_{re,1}$ stage, the discrepancy between V/V_0 and V_{eff}/V_0 gets more obvious, owing to the enhanced vorticities on the distorted bubble interface and the strengthening bubble-wall interaction, as shown in Fig. 7, which strengthens the mixing between the ambient air and the SF_6 gas. For case 2, owing to a shorter end wall distance L, the time interval between I_{in} and $I_{re,2}$ is short, and the discrepancy between V/V_0 and V_{eff}/V_0 also becomes large gradually for the same reason as that in case 1 behind the reflected shock wave, but owing to the less developed vorticities and the weaker interaction between the distorted SF_6 bubble and the wall in case 2, the increase rate of V/V_0 is smaller than that in case 1 by comparing the purple and cyan lines. It is also worth noting that, during the time period of the reflected shock wave compression ($I_{re,1}$ and $I_{re,2}$), the variation rates remain unchanged basically except for the bubble volume in case 1. The three red short lines with the same slope for the bubble volume and effective bubble volume indicate that the reflected shock wave has a dominant compression effect on the distorted SF_6 bubble despite the different vorticities on the bubble interface in different cases. Nevertheless, for the bubble volume in case 1, the slope of the blue line is not steep compared with those red lines, which implies that the SF_6 bubble-wall interaction plays a vital role in the SF_6 bubble volume evolution compared with the influence of vorticities during this time period. Even so, the decrease owing to the reflected shock wave compression has a stronger influence than the increase owing to the bubble-wall interaction. Hence, generally speaking, the incident and reflected shock waves can both compress the bubble volume and effective bubble volume, but the vorticities on the bubble interface owing to the impingement of the shock wave could promote the mixing of the ambient air and SF_6 to increase the bubble volume. Moreover, the interaction between the distorted bubble and the wall also has a significant influence on the increase in the bubble volume, especially for case 1 with a longer end wall distance and a stronger bubble-wall interaction, which indicates the three-dimensional effect of the computational domain again and the influence of the end wall distance.

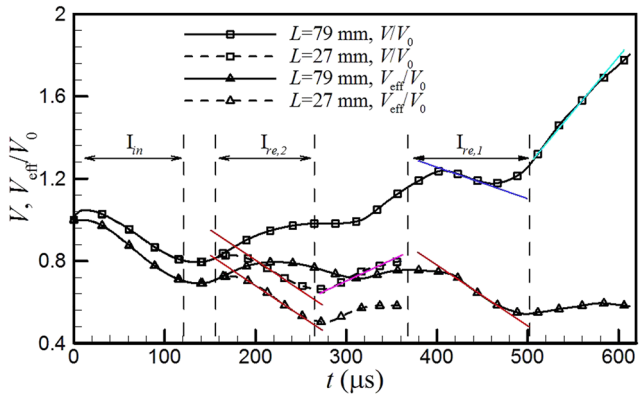

FIG. 11. Evolution of the bubble volume and effective bubble volume.

IV. CONCLUSIONS

In this study, a detailed three-dimensional numerical investigation of the interaction between the incident and reflected shock waves and the spherical SF_6 gas bubble is conducted using the high-order numerical schemes. The influences of the end wall distance on the evolution of the distorted SF_6 gas bubble are also clarified. The results indicate the three-dimensional effects of the computational domain, and the main conclusions are summarized as follows:

(1) For case 1, the vorticities mainly emerge at the interfaces of the shock wave and SF_6 bubble, and the high pressure impingement and the induction of downstream vorticities caused by the incident shock wave can both promote the formation of the downstream jet. When the reflected shock wave interacts with the SF_6 bubble again, the distorted SF_6 bubble is further compressed, and more vorticities emerge at the bubble interface. From the view of the three-dimensional SF_6 bubble structure, big vortices of the SF_6 bubble interact with the walls in the y-direction, and an obvious increase in the bubble volume is observed. Also, small vortices emerge on the headmost and adjacent locations of the jet.

(2) For case 2 with a short end wall distance, the reflected shock wave impinges on the distorted SF_6 bubble during the budding stage of the downstream jet (Jet-R) formation, which induces a short and wide jet. Also, the distorted SF_6 bubble is not flat like that in case 1; thus, a new upstream jet (Jet-L) emerges during the impingement of the reflected shock wave. In addition, there is no interaction between the distorted SF_6 bubble and the wall in the y-direction until a very late time, so the bubble volume is smaller than that in case 1.

(3) The case with a short end wall distance has less developed vorticities and weaker bubble-wall interaction; thus, the bubble volume and effective bubble volume in case 2 are both smaller than those in case 1, and the discrepancy between the two volumes in case 2 is also smaller. However, for the two cases with different end wall distances, the reflected shock wave has a dominant compression effect on the distorted SF_6 bubble evolution, although the bubble-wall interaction has more significant influence than the influence of vorticities on the bubble volume increase in case 1 with a longer end wall distance and a stronger bubble-wall interaction.

ACKNOWLEDGMENTS

This work was supported by the National Natural Science Foundation of China (Grant Nos. 11872193 and 11402102), the Natural Science Foundation of Jiangsu Province of China (Grant No. BK20140524), the Jiangsu Overseas Visiting Scholar Program for University Prominent Young & Middle-aged Teachers and Presidents, and the Youth Talent Cultivation Plan of Jiangsu University. Supercomputing time on ARCHER is provided by the "UK Consortium on Mesoscale Engineering Sciences (UKCOMES)" under the UK Engineering and Physical Sciences Research Council, Grant No. EP/R029598/1.

REFERENCES

[1] D. Ranjan, J. Oakley, and R. Bonazza, "Shock-bubble interactions," Annu. Rev. Fluid Mech. **43**, 117–140 (2011).
[2] J. F. Haas and B. Sturtevant, "Interaction of weak shock waves with cylindrical and spherical gas inhomogeneities," J. Fluid Mech. **181**, 41–76 (1987).
[3] G. Layes, G. Jourdan, and L. Houas, "Distortion of a spherical gaseous interface accelerated by a plane shock wave," Phys. Rev. Lett. **91**, 174502 (2003).
[4] G. Layes, G. Jourdan, and L. Houas, "Experimental investigation of the shock wave interaction with a spherical gas inhomogeneity," Phys. Fluids **17**, 028103 (2005).
[5] G. Layes, G. Jourdan, and L. Houas, "Experimental study on a plane shock wave accelerating a gas bubble," Phys. Fluids **21**, 074102 (2009).
[6] D. Ranjan, J. H. J. Niederhaus, B. Motl, M. H. Anderson, J. Oakley, and R. Bonazza, "Experimental investigation of primary and secondary features in high-mach-number shock-bubble interaction," Phys. Rev. Lett. **98**, 024502 (2007).
[7] D. Ranjan, J. H. J. Niederhaus, J. G. Oakley, M. H. Anderson, R. Bonazza, and J. A. Greenough, "Shock-bubble interactions: Features of divergent shock-refraction geometry observed in experiments and simulations," Phys. Fluids **20**, 036101 (2008).
[8] T. Si, Z. G. Zhai, J. M. Yang, and X. S. Luo, "Experimental investigation of reshocked spherical gas interfaces," Phys. Fluids **24**, 054101 (2012).
[9] J. H. J. Niederhaus, J. A. Greenough, J. G. Oakley, D. Ranjan, M. H. Anderson, and R. Bonazza, "A computational parameter study for the three-dimensional shock-bubble interaction," J. Fluid Mech. **594**, 84–124 (2008).
[10] D. X. Fu, Y. W. Ma, and X. L. Li, "Direct numerical simulation of three-dimensional Richtmyer-Meshkov instability," Chin. Phys. Lett. **25**, 188–190 (2008).
[11] Y. J. Zhu, G. Dong, B. C. Fan, and Y. X. Liu, "Formation and evolution of vortex rings induced by interactions between shock waves and a low-density bubble," Shock Waves **22**, 495–509 (2012).
[12] B. Hejazialhosseini, D. Rossinelli, and P. Koumoutsakos, "3D shock-bubble interaction," Phys. Fluids **25**, 091105 (2013).
[13] B. Rybakin and V. Goryachev, "The supersonic shock wave interaction with low-density gas bubble," Acta. Astronaut. **94**, 749–753 (2014).
[14] J. Yang, Z. H. Wan, B. F. Wang, and D. J. Sun, "Numerical simulation of shock bubble interaction with different Mach numbers," Chin. Phys. Lett. **32**, 034701 (2015).
[15] Z. G. Zhai, T. Si, X. S. Luo, and J. M. Yang, "On the evolution of spherical gas interfaces accelerated by a planar shock wave," Phys. Fluids **23**, 084104 (2011).
[16] Z. G. Zhai, T. Si, L. Y. Zou, and X. S. Luo, "Jet formation in shock-heavy gas bubble interaction," Acta. Mech. Sin. **29**, 24–35 (2013).
[17] Y. J. Zhu, L. Yu, J. F. Pan, Z. H. Pan, and P. G. Zhang, "Jet formation of SF_6 bubble induced by incident and reflected shock waves," Phys. Fluids **29**, 126105 (2017).
[18] Y. J. Zhu, Z. W. Yang, Z. H. Pan, P. G. Zhang, and J. F. Pan, "Numerical investigation of shock-SF_6 bubble interaction with different mach numbers," Comput. Fluids **177**, 78–86 (2018).
[19] Y. J. Zhu, Z. W. Yang, K. H. Luo, J. F. Pan, and Z. H. Pan, "Numerical investigation of planar shock wave impinging on spherical gas bubble with different densities," Phys. Fluids **31**, 056101 (2019).
[20] G. S. Jiang and C. W. Shu, "Efficient implementation of weighted ENO schemes," J. Comput. Phys. **126**, 202–228 (1996).
[21] V. N. Gamezo, E. S. Oran, and A. M. Khokhlov, "Three-dimensional reactive shock bifurcations," Proc. Combust. Inst. **30**(2), 1841–1847 (2005).